

# Contents lists available at ScienceDirect

# Acta Materialia

journal homepage: www.elsevier.com/locate/actamat



Full length article

# Mechanical degradation due to vacancies produced by grain boundary corrosion of steel



Denizhan Yavas<sup>a</sup>, Thanh Phan<sup>a</sup>, Liming Xiong<sup>a</sup>, Kurt R. Hebert<sup>b</sup>, Ashraf F. Bastawros<sup>a,\*</sup>

- <sup>a</sup> Department of Aerospace Engineering, Iowa State University, Ames, IA 50011-2271, United States
- <sup>b</sup> Department of Chemical Engineering, Iowa State University, Ames, IA 50011-2271, United States

#### ARTICLE INFO

Article history:
Received 4 July 2019
Revised 15 July 2020
Accepted 30 August 2020
Available online 11 September 2020

Keywords:
Nanoindentation
Atomistic modeling
Grain boundary degradation
Stress corrosion cracking
Vacancies
Dislocation activation volume

# ABSTRACT

Ductile alloys fail in corrosive environments by intergranular stress corrosion cracking, through interactions between mechanical and chemical processes that are not yet understood. We investigate formation and mechanical effects of metal defects produced by grain boundary corrosion of low-alloy pipeline steel, at conditions of high susceptibility to stress corrosion cracking in the absence of hydrogen evolution. Nanoindentation measurements show local softening near corroded grain boundaries, indicated by significantly reduced critical loads for dislocation nucleation. Molecular dynamics simulations of nanoindentation of bulk iron showed that metal vacancies and not interstitial hydrogen atoms explain the observed critical load reduction. Both the dislocation activation volume and dislocation activation energy for vacancy-charged samples are found to be nearly one-half of that for a hydrogen charged samples. Quantitative agreement with experimentally measured indentation response was found for vacancy concentrations equivalent to the bulk silicon concentration in the steel, suggesting that vacancies originate from oxidation of reactive silicon solute atoms at grain boundaries. The results help explain the chemical mechanism of formation of vacancy defects that may participate in grain boundary degradation in the absence of hydrogen embrittlement environment.

© 2020 Acta Materialia Inc. Published by Elsevier Ltd. All rights reserved.

# 1. Introduction

Stress corrosion cracking (SCC) is the unexpected fracture in corrosive environments of normally ductile metallic alloys. In intergranular stress corrosion cracking (IGSCC), grain boundaries (GBs) define the active pathways for crack growth. IGSCC affects technologically critical materials such as steel for oil and gas pipelines and aluminum alloys for aircraft [1]. The fundamental interaction of corrosion and mechanical degradation in IGSCC is not completely understood. IGSCC processes at near-ambient temperatures are often explained in terms of heightened chemical susceptibility at grain boundaries due to impurity segregation or secondphase precipitation [2,3], selective dissolution of reactive alloy constituents to form mechanically weak porous layers [4], or hydrogen absorption during corrosion at low potentials [5]. The present work focuses on a system that does not fit this typical phenomenology, namely the initiation stage of IGSCC of low-carbon pipeline steels in "high pH" aqueous carbonate-bicarbonate solutions (pH 8-10) [6]. IGSCC occurs at potentials of active steel dissolution, significantly higher than the potential range of hydrogen evolution, and

crack velocities correlate with metal dissolution rates [7–10]. For these reasons, it is thought that crack initiation and growth are not affected by absorbed hydrogen. Also, microscopic characterization studies do not reveal second-phase particles or segregated impurities at grain boundaries [11,12], nor evidence of porous metallic layers after corrosion [12].

IGSCC of pipeline steels is preceded by an initiation stage of selective grain boundary attack or intergranular corrosion (IGC). Recently, we reported detailed nanoindentation (NI) measurements across grain boundaries of a X70 pipeline steel after high-pH IGC [13]. The measurements revealed distinct hardness reductions up to about 25% relative to the grain interiors but no significant change in elastic modulus within distances of 1 µm from corroded GBs. These results constitute direct evidence for corrosion-induced grain boundary softening. We suggested that the local softening arises from synergistic interactions between the dislocation nucleation process and a "softening agent" such as hydrogen interstitials or lattice vacancies [14-17]. Since H absorption was considered unlikely due to the high electrochemical potential, it was suggested that softening may derive from vacancies generated by oxidation of reactive Si solute atoms in X70 steel [12,18]. The large overpotential of 0.8 V for Si oxidation at steel dissolution potentials can overcome the kinetic barrier for dissolution of terrace atoms as op-

<sup>\*</sup> Corresponding author.

E-mail address: bastaw@iastate.edu (A.F. Bastawros).

posed to kink or step atoms, a necessary condition for vacancy injection [19]. Thus, vacancy formation by Si oxidation could provide a plausible chemical mechanism for corrosion-induced localized plasticity at grain boundaries. Evidence in the context of hydrogen embrittlement suggests that vacancies generated by dislocation plasticity in the presence of hydrogen can promote GB cracks [20–24]. This suggests that corrosion-generated vacancies may help explain GB embrittlement, despite ductile crack-tip shielding arising from vacancy-induced dislocation activity.

The present work attempts to identify the defects responsible for near-GB softening and elucidate the chemical mechanism of their formation. The NI results of Ref. [13] are interpreted with the help of molecular dynamics (MD) simulations of the indentation experiments. The simulations approximate the experiments on low-alloy ferritic steel through nanoindentation of iron bcc single crystals with variable concentrations of either vacancies or interstitial hydrogen atoms. In fact, hydrogen should play no direct role in softening in our experiments because the H concentration at the experimental conditions is very small (see Appendix A for a quantitative justification). We include simulations of hydrogen effects as a benchmark for comparison to the vacancy simulations, in view of experimental evidence that H induces softening at sufficiently high concentrations [16,17]. The hydrogen studies may also help elucidate hydrogen-induced SCC at more negative potentials than that used in this work [6]. Also, the simulations do not consider vacancy-hydrogen defects formed by energetically favorable binding of vacancies to hydrogen in Fe, which can aggregate to create proto nano-voids [24]. As argued in Appendix A, the concentration of vacancy-hydrogen defects should not be significant in our experiments, in view of the very small H concentration. The numerical work only considers H or vacancies already present at GBs prior to nanoindentation, and therefore does not include long-range diffusion of H or vacancies during the indentation loading process.

The simulated and experimentally measured NI responses are compared to determine the relative roles of hydrogen vs. vacancies in modulating the critical stress for dislocation nucleation. The main experimental findings from Ref. [13] are first presented as load-displacement curves at variable distance from corroded GBs. These results are then compared to MD-simulated loaddisplacement curves for variable H and vacancy concentrations. To further elucidate on the role of vacancies vs. hydrogen on dislocation nucleation, a range of loading rates and temperatures are also simulated to evaluate the variation of the dislocation activation volume. A model for defect diffusion is provided to directly compare the experimental and simulated NI results on the basis of the hypothesis of vacancy injection by Si oxidation. Conclusions are drawn on the mechanism of corrosion-induced local plasticity. This investigation illustrates that the present approach using nanoindentation coupled with MD can identify defects involved in degradation and elucidate the chemical mechanism of their forma-

# 2. Experimental and theoretical methods

### 2.1. Nanoindentation experiments

Samples of a high strength low carbon steel (API 5L X70) were used in the corrosion experiments. The primary alloying elements were Mn (1.70 wt%), Si (0.37 wt%), Cr (0.06 wt%) and C (0.09 wt%). The majority ferrite phase consisted of nearly equiaxed grains with about 5  $\mu$ m average grain diameter, while the minority pearlite phase was composed of elongated grains less than 5  $\mu$ m in width. The steel specimens were polished to 800 grit finish, cleaned and mounted in an electrochemical cell with a Ag/AgCl reference electrode and Pt counter electrode (cited potentials are with respect to Ag/AgCl). The test solution was 1 M NaHCO<sub>3</sub> at pH 8.1 at room

temperature. A potential of -1.0 V was applied for 5 min to cathodically reduce surface oxide, and then the potential was stepped to a value of -0.521 V within the active dissolution region of the current-potential curve, and held at this level for 2 h. The corroded steel samples were polished at shallow angles relative to the original surface to reveal cross sections through the intergranular corrosion layer in order to enable nanoindentation testing around grain boundaries. The polishing angle was estimated as 0.06° by measurement of the apparent corrosion product layer thickness [13]. Special care was taken to ensure that the surface roughness was significantly smaller than the indenter tip radius. The average root mean square (RMS) geometric roughness for each indentation site was measured to be smaller than 5 nm over  $200 \times 200 \text{ nm}^2$ , a level which would not affect subsequent NI. Nanoindentation tests used a Hysitron TI 950 Tribolndenter with a 90° cube corner diamond indenter tip with a tip nose radius of about 300 nm. Multiple lines of shallow indents were imposed perpendicular to a GB and 1  $\mu$ m apart. Within each line, indents with 250  $\mu$ N peak load were spaced at 0.5  $\mu$ m intervals to avoid overlap of the indentation process zones [25,26]. A height topological scan is generated by the indenter tip and shown in Fig. 2(a). Further experimental details are available elsewhere [12,13,18,27].

#### 2.2. Molecular dynamics simulations

Molecular dynamics calculations to simulate the indentation experiments were performed on a domain representing an iron bcc single crystal. The computational cell with dimensions  $150 \times 150 \times 75$  Å enclosed 143,312 atoms. The atomistic simulator LAMMPS was employed for MD calculations [28]. Two interatomic potentials based on the embedded atom method were utilized for iron-iron and iron-hydrogen interactions [29,30]. The results were analyzed using the dislocation analysis tool in OVITO [31]. Different vacancy concentrations in the range 0-1 at.% were realized by random deletion of Fe atoms from the perfect lattice. Interstitial H atoms were randomly introduced into the perfect lattice at selected interstitial sites [32,33]. Prior to indentation, the atomistic models were relaxed at a constant temperature of 1 K for 50 ps, under the canonical ensemble (constant volume and temperature). The low temperature was imposed to ensure immobility of the introduced vacancies. Periodic boundary conditions were used along the <100> and <010> directions, while non-periodic and shrinkwrapped boundary conditions were used in <001> direction. The atoms within the bottom layer of the model with thickness 10 Å were rigidly fixed. For each vacancy or hydrogen concentration, six different initial configurations were generated and analyzed to characterize the statistical variation of the simulation results.

Nanoindentation simulations were performed using a rigid spherical indenter with radius R=50 Å up to an indentation depth of 20 Å, under the micro-canonical ensemble (constant volume and energy). Although the temperature was initially set to 1 K, a very small temperature fluctuation with a peak of 3 K was recorded during the indentation loading stage. The indentation axis was chosen to be along the <001> direction. The initial position of the indenter was located at the center of the simulation cell. The indenter applied a force on each atom in the material sample with magnitude

$$F(r) = \begin{cases} -K(r-R)^2, & r < R \\ 0, & r \ge R \end{cases}$$
 (1)

where R is the indenter radius, r is the distance between the indenter center and the atom, and the constant K is 10 eV/Å<sup>2</sup>. The indenter speed of 5 m/s was applied with a time step of 2 fs. It should be noted that the indentation speed of the simulations is relatively high compared to the experiments, though it is sufficiently low to maintain the equilibrium state in the simulations

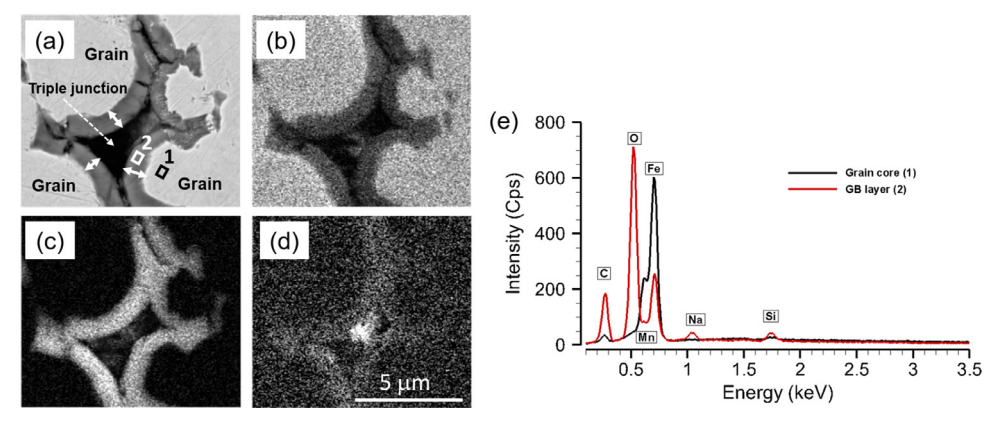
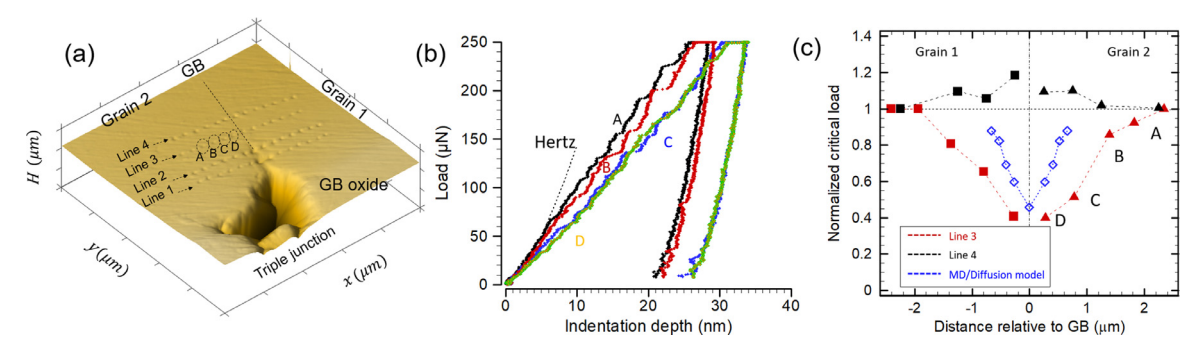


Fig. 1. (a) SEM image of the angle-polished corroded surface, showing the IGC attack at a triple junction. (b-d) EDS intensity maps showing Fe, O, and Si content, respectively. (e) EDS spectra on the selected regions 1 and 2 marked in (a).



**Fig. 2.** (a) AFM image in surface gradient mode showing the grain boundary and the locations of the imposed lines of nanoimprints. (b) A representative set of load-indentation depth curves for the indents on line 2 at different distances from the GB, along with Hertzian fit for the spherical contact. (c) The variation of the critical load for the first displacement burst (normalized by the critical loads obtained for the interior of the grains) with the distance from the GB, along with the predictions of the MD/vacancy diffusion model (Eq. (5)).

and qualitatively achieve the targeted results. In this work we utilize the first displacement burst to identify the critical nucleation stress for dislocation. The inclusion of vacancies or H into the crystal might favor heterogeneous mechanisms of dislocation nucleation, and thereby their activation volume [34]. To clarify such effects, MD simulations of two sets of samples containing the same concentration of initially introduced H-interstitials and vacancies are examined under nanoindentation with strain rates of  $10^8/s$ ,  $10^9/s$ , and  $10^{10}/s$  and at temperatures of 100K, 300K, and 500K.

# 3. Results and discussion

# 3.1. Nanoindentation experiments

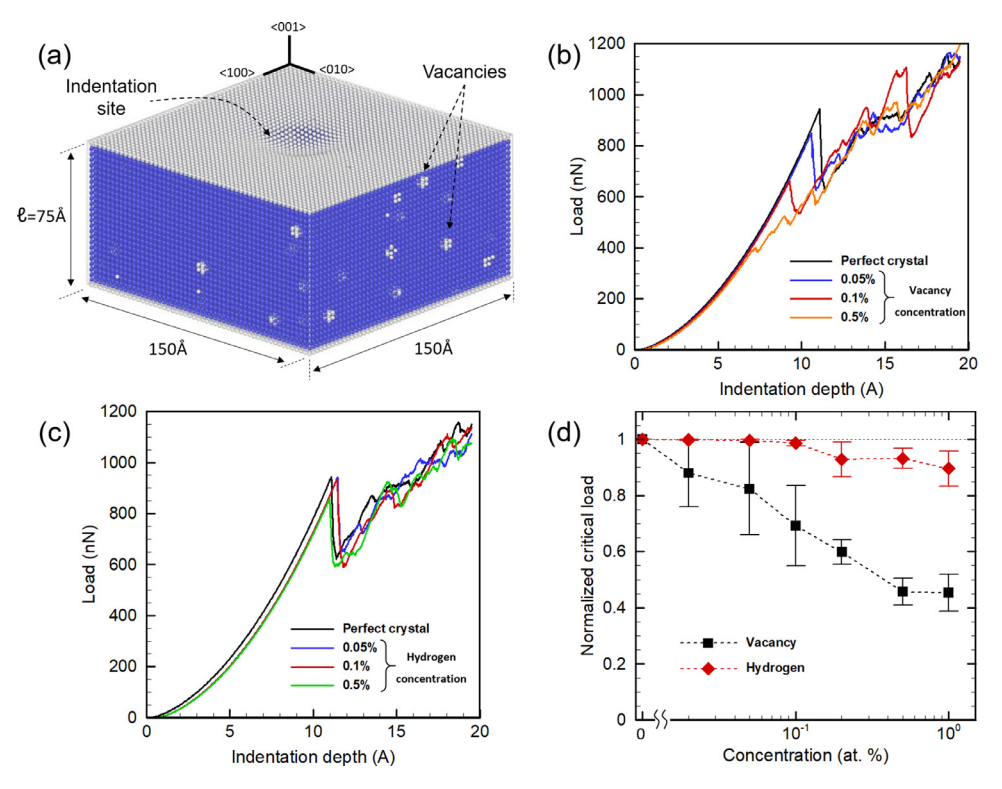
The SEM micrograph in Fig. 1(a) illustrates the morphology of the subsurface intergranular corrosion layer revealed by shallowangle polishing. The light gray-shaded regions are the roughly equiaxed ferrite grains. IGC attack produced crevices at triple junctions shown as black-shaded areas surrounded by approximately 1  $\mu$ m thick dark gray-shaded oxide-carbonate corrosion product layers [12]. Fig. 1(b-d) depicts the energy-dispersive X-ray spectroscopy (EDS) elemental intensity maps for Fe, O, and Si contents, respectively. The GB corrosion product layer is mainly composed of Fe and O. Fig. 1(e) shows EDS spectra for region 1 within grain interior and region 2 within GB corrosion product layer, as highlighted in Fig. 1(a). The EDS spectra shows the presence of Si in the GB corrosion product layer, thus demonstrating oxidation of Si solute atoms at grain boundaries.

Fig. 2(a) is an atomic force microscope (AFM) surface topography scan showing a crevice at the GB triple junction, with four

lines of NI imprints across the GB at different distances from the triple junction. Lines 2 and 3 are close to the GB crevice, where an approximately 1  $\mu$ m thick corrosion product should be found based on SEM images as in Fig. 1 (a). The corrosion product layer at line 3 should be much thinner than 1  $\mu$ m, and line 4 is beyond the maximum penetration of corrosion. Fig. 2(b) shows a set of load-indentation depth curves at the different locations indicated in Fig. 2(a). The initial elastic Hertzian contact response of the base material is also marked on Fig. 2(a) for indentation modulus (E=210 GPa) and indenter tip radius (R = 350 nm) [35]. Within the first few nanometers, all curves exhibited similar responses that follow Hertzian contact behavior.

All indentation curves exhibited multiple displacement bursts. Displacement bursts have been linked with several different mechanisms such as dislocation nucleation or propagation [36–38], brittle cracking of the native oxide layer [39], and surface roughness [40]. In this work, we ensured that the surface roughness (~5nm) is much smaller than the NI tip radius. Therefore, the first displacement burst event on every curve can be safely considered as the dislocation load at H/vacancies, when the critical nucleation stress is reached underneath the indenter tip [36–38]. The critical stress required to nucleate a homogenous dislocation loop  $\tau_{cr}$  occurs at the maximum shear stress underneath the indentation surface  $\tau_{max}|_{burst}$ . This stress level can be assessed from the critical load associated with the first displacement burst event, and is given by

$$\tau_{cr} \approx \tau_{\text{max}}|_{burst} = 0.31 \left( \frac{6 E^2}{\pi^3 R^2} P_{burst} \right)^{1/3}$$
(2)



**Fig. 3.** (a) MD simulation model, showing the iron atoms (blue), and the atoms surrounding the lattice vacancies (0.1 at.%). (b) Load-indentation depth curves for different vacancy concentration, (c) load-indentation depth curves for different hydrogen atom concentration. (d) The MD results for the critical dislocation nucleation load (normalized by that of perfect crystal) as a function of the concentration. The error bar is derived from six different geometric rendering of the model.

where  $P_{burst}$  is the measured load corresponding to the first displacement burst [36]. Fig. 2(c) shows the spatial variation of the average of  $P_{burst}$  within the two grains along lines 3 and 4 as a function of distance from the GB. Loads were normalized by that of the grain interior. On line 3 (which will be compared with the MD simulation), a 55-60% drop is detected in  $P_{burst}$  near the GB compared to the bulk of the grains. From Eq. (2), this implies an approximately 25% degradation in the barrier stress  $\tau_{cr}$  level for dislocation nucleation, and therefore an enhanced plasticity with a lower dislocation nucleation barrier. Line 2 (not shown here) exhibited nearly the same spatial modulation as line 3, but with a lateral shift corresponding to the thickness of the GB corrosion product. The observed trend of  $P_{burst}$  modulation was found at other triple junctions on the same surface, with a spatial modulation zone 1-2  $\mu m$  from the GBs. To highlight the significance of the observed reduction in  $P_{burst}$  close to corroded GBs, note that line 4, located beyond the corrosion-affected region, exhibits the opposite trend of  $P_{burst}$  with increased levels close to the GB. Other sets of NI scans on uncorroded surfaces showed statistical variations of  $P_{burst}$  with similar increased levels closer to the GB. Such increases are typically understood in terms of increase of barrier stress for dislocation nucleation close to GBs [40].

# 3.2. Molecular dynamics simulations

MD simulations using the embedded atom method were employed to explore the roles of hydrogen and vacancy defects in the NI response, and to identify the atomistic mechanisms responsible for corrosion-induced softening near the GB. Nanoindentation on domains representing bcc Fe single crystals was compared to the response of the same domains with various concentrations of either vacancies or hydrogen. Fig. 3(a) shows the starting configu-

ration of the atomistic model cell for 1% (atomic percent) vacancy concentration, with light shading used to highlight atoms neighboring vacancies. Fig. 3(b) shows the load-indentation depth curves for three different vacancy concentrations, along with the perfect crystal response. The initial elastic response of the crystal showed a minor gradual softening with increase of the atomic vacancy concentration. All loading curves exhibited load bursts at critical loading levels that tended to decrease with increasing vacancy concentration. Simulations produced load rather than displacement bursts as in Fig. 2(b), since the displacement rate was controlled. For perfect crystal, simulation results showed that multiple dislocations nucleated simultaneously, yielding a large load burst. However, with increase of the vacancy concentration, successive and discrete dislocation nucleation events were observed, leading to gradual stair-case bursts as shown in the curve for 0.5% vacancy concentration. It is worth noting that all the load-indentation depth curves exhibited the same average slope after exhaustion of the load burst events, due to a similar lattice resistance for dislocation mobility. This trend confirms that these dispersed atomic-scale vacancies, differently from nanoscale vacancy clusters which usually act as obstacles to dislocation migration, can reduce the dislocation nucleation barrier, while they may not significantly impact dislocation migration kinetics. Fig. 3(c) shows the load-indentation depth curves for different H atomic concentrations, along with the curve for the perfect crystal for comparison. There was an observable softening within the initial elastic part of the curves compared to that for the perfect lattice. However, no distinct change was found relative to the perfect crystal for either the critical load or the amplitude of the load bursts.

Fig. 3(d) summarizes the nucleation load as a function of the concentration of both H and vacancies. Clearly, the presence of va-

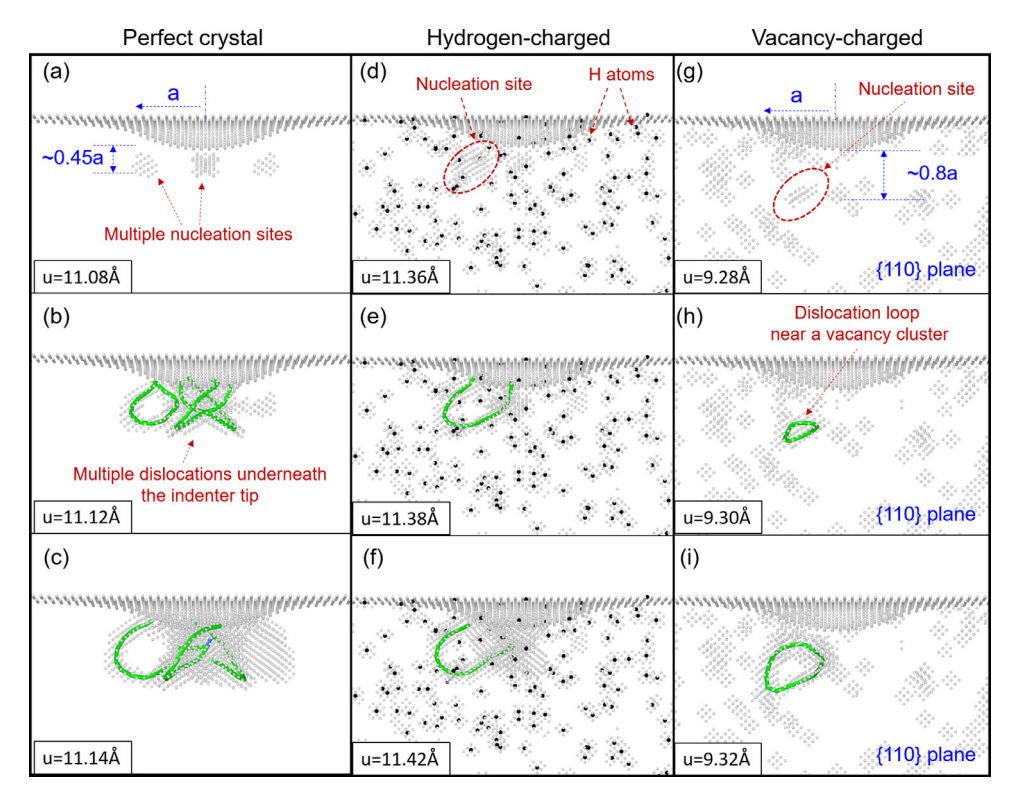


**Fig. 4.** Atomistic simulation results showing dislocation nucleation and propagation at the critical loading level. Snapshots of atomistic projection with shading of out-of-registry atoms for the perfect crystal (a-c), hydrogen interstitial (d-f), and vacancy cases (g-i), highlighting the variation of dislocation nucleation characteristics with addition of lattice vacancies and H interstitials. H and vacancy concentration at 0.1 at.%.

cancies leads to a noticeable reduction of the critical load for the initial load burst. In contrast, interstitial H has an insignificant effect (within 10% for 1 at.% concentration) on the critical load for dislocation nucleation. This trend leads to the conclusion that vacancies rather than interstitial H atoms act as softening agents under these particular conditions. Similar simulations were also performed for double-sized samples under indentation. Similar trends to those in Fig. 3(d) were observed, eliminating the possibility of artifacts due to the limited sample size in the MD model.

Fig. 4 depicts atomic-scale events during dislocation nucleation and propagation for a perfect crystal in Fig. 4(a-c), 0.1% H concentration in Fig. 4(d-f), and for 0.1% vacancy concentration in Fig. 4(g-i). Each column shows atomistic projections with shading of out-of-registry atoms. Panels (a), (d), and (g) represent the initial Hertzian deformation field, prior to appearance of dislocations; (b), (e), and (h) show the simulation cell immediately after the first dislocation nucleation event, while (c), (f), and (i) represent a later stage showing slight evolution of the nucleated dislocation loops.

For the case of the perfect crystal, Fig 4 (a-c) shows that multiple dislocation loops nucleated under the indenter tip, where the maximum shear stress reached the theoretical strength of the lattice. In the simulation shown in Fig. 4(a), three nucleation sites were activated by indentation, highlighting the bcc crystal symmetry. The depths of the nucleation sites are approximately 45% of the contact radius a, measured along the indenter line of symmetry from the indenter-crystal interface. The dislocation nucleation site is close to the depth of 0.48a for maximum shear stress under spherical contact predicted by Hertzian analysis [35]. Once these dislocation loops nucleated, they migrated under the increasing applied load until intercepting the indenter interface (Fig. 4(b, c)). For 0.1% H concentration, dislocation nucleation exhibits a similar trend as the perfect crystal, except only one of the {110} slip planes was activated. Fig. 4(d) shows the atomistic configuration immediately before dislocation nucleation, where black-shaded H atoms are surrounded by gray-shaded out-of-registry atoms. Although there are multiple H atoms underneath the indenter tip, a single dislocation nucleated under the indenter, at a depth of 0.52a close to that expected for the perfect crystal. The location of the first dislocation nucleation was approximately independent of H atom sites for this particular concentration; however, the existence of H provided preferential nucleation sites for single dislocations by distorting the deformation symmetry. For 0.1% vacancy concentration in Fig. 4(g), out-of-registry atom clusters representing atomic relaxations around individual vacancies are present prior to contact with the indenter. Fig. 4(h) reveals that the first dislocation loop nucleated close to such a vacancy site. The depth of this nucleation site is about 84% of the contact radius a, much larger than 0.48a for the perfect crystal case. Thus, the local shear stress at this site would be below that for the first dislocation nucleation in the absence of vacancies (Fig. 4(g)). Apparently, the energy barrier for nucleation was reduced at vacancy sites relative to that for the perfect crystal; however, H defects did not lower the barrier significantly. Once nucleated, the dislocation loop grew under the applied load (Figs. 4(i)).

The ability of vacancies but not hydrogen to reduce the energy barrier for dislocation nucleation correlates with the local atomic configuration around defects in the relaxed state before indentation. Figs. 5 (a) and (b) compare the first strain invariant (associated with hydrostatic strain) around a vacancy and H atom on the {001} plane in the relaxed state. Fig. 5(c) shows the distribution of the first strain invariant along the <110> direction, noted on Fig. 5(a, b). In the 0.1% vacancy case, the overall model experiences a tensile (dilation) residual volumetric strain of about 0.40% after relaxation around vacancies. On the other hand, in the 0.1% H case, there is a compressive residual volumetric strain about 0.45% after relaxation around H atoms. MD simulations of the effect of volumetric pre-strain up to 1% on nanoindentation behavior in nickel and palladium single crystals showed that a tensile

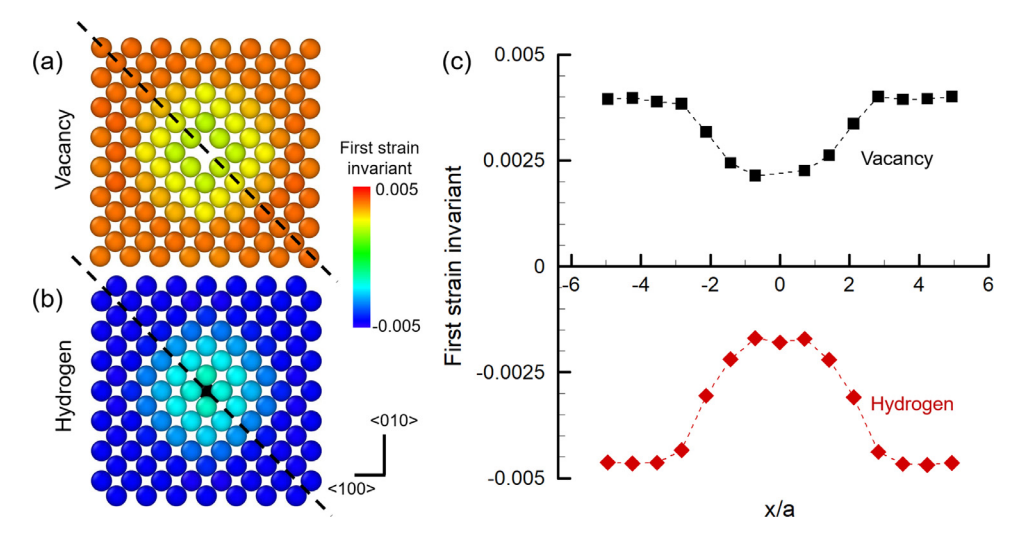


**Fig. 5.** Distribution of first strain invariant on {001} plane, showing initially induced hydrostatic strain by (a) a vacancy and (b) hydrogen atom. (c) The line distribution of first strain invariant along <110> direction (marked by the dashed lines on (a) and (b)) presented as a function of distance normalized by the atomic distance. H and vacancy concentration at 0.1 at.%.

pre-strain reduced pop-in load, while a compressive lattice strain increased pop-in load [41]. Our results are consistent with these observations, except that the present Fe-H system does not exhibit an increase in the pop-in load even though it shows a compressive residual strain.

# 3.3. Estimates of dislocation activation volume under the presence of defects

The objective of this computation is to provide quantitative evidence showing the significant difference between hydrogen interstitials and vacancies on how they affect the crystal to favor heterogeneous mechanisms of dislocation nucleation, and thereby the dislocation activation volume [34]. The dislocation activation volume is measured through a series of indentation simulations at a wide range of strain rates and temperature. The two sets of configurations containing the same concentration of initially introduced hydrogen interstitials and vacancies of 0.1 at.% are indented under  $10^8/s$ ,  $10^9/s$ , and  $10^{10}/s$ , at temperatures 100K, 300K, and 500 K. The atomistic model setup and the obtained load-indentation depth curves for the simulations at T = 300K are shown in Fig. 6.

Fig. 6 shows several unique attributes of the effect of both Hinterstitials and vacancies on the load-indentation depth curves: (1) For the shallow indentation range (h < 7.5 Å), dislocation nucleation does not occur. Both samples are within the elastic deformation stage and exhibit the same constitutive response in terms of the load- indentation depth curves. Again, this implies that the elastic properties of the hydrogen- and vacancy-charged samples are nearly identical, as noted also on Fig. 3. (2) With the increase of indentation depth, dislocations nucleate in both cases. However, the critical nucleation load increases with the increasing strain rate. (3) Regardless of the applied strain rate, the critical loads at which dislocations nucleate in the vacancy-charged sample (Fig. 6b) are always lower than those in the hydrogen-charged sample (Fig. 6a). It should also be noted that while Fig. 6 shows results at 300K, these three major findings were repeatablein the other simulations at 100K, and 500K.

Using a series of the load- indentation depth curves obtained from the indentation simulations at different strain rates and temperature, we then calculate the dislocation activation volume,  $V_a$  using the widely utilized relation [41–45]:

$$V_a = k_B T \left. \frac{\partial \ln \dot{\varepsilon}}{\partial \tau_{cr}} \right|_T. \tag{3}$$

Here  $k_B$  is the Boltzmann constant, T is the temperature,  $\dot{\varepsilon}$  is the strain rate. The strain rate is estimated as  $\dot{\varepsilon} = v_i/\ell$ , where  $v_i$  is the indentation speed and  $\ell$  is the dimension of the sample along the indentation direction. This may not be exactly accurate but is considered as a reasonable approximation, and is widely used in indentation simulations or experiments [41,42].  $\tau_{cr}$  is the critical shear stress on the slip plane where the dislocation nucleate, and is estimated through Eq. (2), in which  $P_{burst}$ , the critical indentation load at which dislocations start to nucleate, can be directly extracted from the simulated force-indentation depth curves as shown in Fig. 6. A combination of Eq. (2) and (3) enables us to measure the dislocation activation volume from the above simulations of indentation at different strain rates and temperature. In addition to the activation volume, the dislocation activation energy,  $\Delta H^*$  is also estimated using the following equation through an analysis of the results from constant strain rate over different temperatures:

$$\Delta H^* = -V_a T \left. \frac{\partial \tau_{cr}}{\partial T} \right|_{\dot{E}}. \tag{4}$$

Table 1 lists the dislocation activation volumes together with the activation energy estimated from our atomistic simulations. Here, the activation energy is calculated from the simulations at a constant strain rate of 108/s. Clearly, at all three different temperatures, the energy required for activating dislocations in a sample containing vacancies is always lower than that in a H-charged sample. The same trend has also been found in all the other simulations at strain rates of 109/s and 1010/s. This result confirms that the presence of vacancies promotes dislocation nucleation more the interstitial hydrogen does. Moreover, the dislocation activation volumes listed in Table 1 are at the same level as that ( $\sim 4b^3$  for dislocation nucleation in perfect single crystalline bcc iron) in many previous MD simulations [34,43-45] and even a few experimental results [46,47], but significantly differ from that ( $\sim 10 \, b^3 - 1000 \, b^3$ ) in many other experiments [48–50]. One main reason is that the dislocation activation volume in materials is not a constant, but rather always scatters due to its dependence on dislocation character (edge, screw, or mixed), strain rates, grain size, temperature, chemical impurities, and among other factors. Other significant differences between experiments and MD simulations include the following: (i) A higher strain rate usually leads to a smaller dislocation activation volume. The lowest strain rate in the present MD is at a level of ~108/s, which is orders of mag-

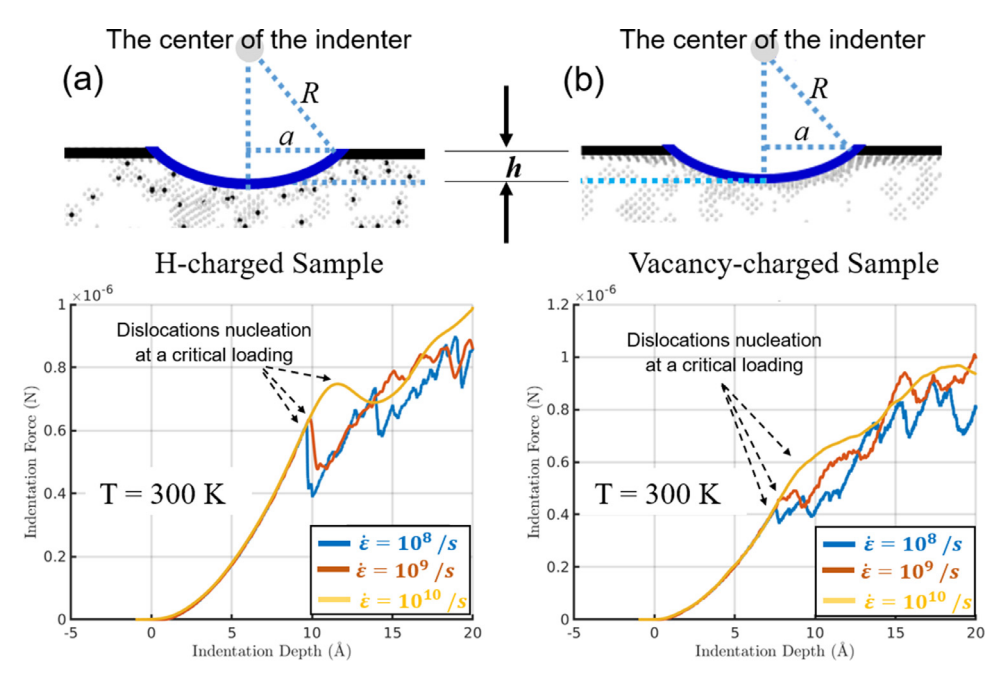


**Fig. 6.** The MD simulation model and the force-depths curves of single crystalline  $\alpha$ -Fe containing (a) hydrogen interstitial and (b) vacancies under a spherical indentation with different strain rates ranging from 10<sup>8</sup> /s to 10<sup>10</sup> /s at T = 300K. Here the same concentration of hydrogen interstitials and vacancies of 0.1 at.% has been initially introduced; R is the radius of the spherical indenter; h is the indentation depth.

**Table 1**Dislocation activation volume and activation energy from the indentation simulations at different temperature (b is the Burgers vector of bcc iron, 0.248 nm).

	T = 100K	T = 300K	T = 500K
$V_a/\Delta H^*$ (H-charged sample)	1.2 b <sup>3</sup> /0.05 eV	1.9 b <sup>3</sup> /0.24 eV	2.6 b <sup>3</sup> /0.57 eV
$V_a/\Delta H^*$ (sample with vacancies)	0.5 b <sup>3</sup> /0.02 eV	1.6 b <sup>3</sup> /0.13 eV	1.9 b <sup>3</sup> /0.26 eV

nitude higher than that  $(\sim 10^{-3}/s)$  in experiments [13,48–51] and in turn, results in a significantly smaller dislocation activation volume. (ii) A smaller grain size always gives rise to a smaller dislocation activation volume [42]. The sample size in the present atomistic model is at the nanometer level but the grain size in experiments is at the micrometer level. With such a huge gap between the MD simulation and experimental length scale, it is not surprising that the activation volume from MD is much smaller than that from experiments. (iii) The more chemical impurities, the more pinning points, and the larger dislocation activation volume [45]. No chemical impurity has been introduced in the present MD model. Thus, the activation volume from simulation, of course cannot be directly comparable with that from experiments in which the sample always contains certain impurities. Obviously, if an experimentally comparable activation volume is desired from a computer simulation, the length scale gap between MD and experiments needs to be filled. We argue that our concurrent atomisticcontinuum (CAC) method [52–57] is one most suitable, if not the best, approach to achieve this goal. At a fraction of the cost of the full MD simulations, with the interatomic force field as the only constitutive rules, CAC was demonstrated to be applicable for: (a) modeling the nucleation and growth of a micron-sized dislocation loop with its atomistic core structures being retained [52,53]; (b) measuring the barrier strength of an atomic-scale obstacles to a  $\mu$ m-long dislocation line [54]; and (c) predicting the reactions between a large number of dislocations and GBs in micron-sized polycrystalline metals [55]. It thus provides a platform for measuring the dislocation activation volume in materials with a microstructure complexity at the experimentally comparable length scale.

Despite the length scale mismatch between the present MD models and experiments, the data in Table 1 show critical aspects of the role of heterogeneous nucleation on impacting our main results: (1) For both the hydrogen- and vacancy-charged samples, the dislocation activation volume increases with the increase in temperature. It implies that a significantly larger number of atoms will get involved in a dislocation nucleation event at a high temperature than that in a low temperature. Such trend is expected, as strong thermal fluctuation at a higher temperature enables more atoms to participate in the activation of a dislocation. (2) The dislocation activation volume for samples containing hydrogen changes faster than it does in the sample containing vacancies. And most importantly, (3) at the same temperature, especially at low temperature, the dislocation activation volume in a sample containing vacancies is significantly less than that in the hydrogen-charged sample. For instance, at 100K, the dislocation activation volume  $(0.5 b^3)$  in a sample containing vacancies is less than one-half of that in the H-charged sample  $(1.2 b^3)$ . At low temperature, given the limited contribution from thermal fluctuations, a smaller activation volume means that fewer atoms participate in a dislocation nucleation event, and in turn, a lower external stress is required to activate it. The activation volume and energy calculations demonstrate that vacancies nucleate dislocations more effectively compared to hydrogen interstitials at the same concentration. Thus, in view of experimental evidence that sufficient H concentrations in Fe alloys stimulate dislocation nucleation [17], vacancy-induced softening must be recognized as a viable mechanism. Moreover, as discussed in the Introduction, the very low H concentrations in our experiments preclude hydrogen-induced softening (see Appendix A). It can be concluded from the MD simulations that nucleation at vacancies generated by corrosion can explain the observed GB softening at active dissolution potentials.

# 3.4. Vacancy diffusion calculation

Calculations with a vacancy diffusion model were carried out to further investigate the origin of corrosion-generated vacancies responsible for softening near GBs. The model hypothesizes that vacancies are injected by oxidation of reactive Si solute atoms at grain boundaries. Accordingly, the vacancy concentration distribution near the GB is calculated and, together with the concentration-dependent critical load from MD, used to predict the spatial variation of critical load for direct comparison to the NI results in Fig. 2(c). The evolution of vacancy concentration near the corroding interface is determined by the transient diffusion equation.

$$\frac{\partial C}{\partial t} - \nu_d \frac{\partial C}{\partial x} = D_v \frac{\partial^2 C}{\partial x^2} \tag{5}$$

where C is the vacancy concentration,  $v_d$  is the dissolution velocity of the GB,  $D_v$  is the vacancy diffusivity, x is position relative to the corroding interface and time t is measured from the initiation of corrosion at the GB site. A constant interfacial concentration  $C_{GB}$  is maintained at x=0, which according to the hypothesis is taken as equivalent to the bulk Si concentration of 0.77 at.%. Since the equilibrium vacancy concentration in steel at ambient temperature is negligible relative to  $C_{GB}$ , C is taken as zero far from the interface and at zero time.

Eq. (5) was solved numerically using values of  $5 \times 10^{-17}$  m<sup>2</sup>/s for  $D_v$  [58], and 0.013 nm/s for  $v_d$  [12]. The vacancy diffusion time is a source of uncertainty in these calculations. As a first approximation, we assume that the diffusion time is the same as the time of corrosion at the applied potential. Based on the location of the GB site probed by NI within the IGC layer [12,13], corrosion initiated roughly 18 min prior to the end of the 2 h experiment. From the concentration profile at 18 min, values of x were determined at the vacancy concentrations for which MD simulations were carried out (Fig. 3(d)). Fig. 2(c) compares the resulting theoretical prediction of the normalized critical force vs. distance from the GB to the NI measurements. Interestingly, the normalized load of 0.4 measured close to the GB is nearly the same as that predicted from the value of  $C_{GB}$  derived from the bulk Si concentration. This agreement supports the hypothesis that the vacancies responsible for lattice softening are injected by oxidation of reactive Si atoms. The same mechanism could explain vacancy injection in other alloys that contain solutes with dissolution potentials significantly more negative than the corrosion potential. Fig. 2(c) also shows that the predicted thickness of the zone of reduced critical load is about 1  $\mu$ m, roughly one-half of the experimental thickness. The discrepancy can be attributed to underestimation of the vacancy diffusion distance by the model; diffusion would actually continue on open circuit until vacancies encounter traps such as dislocations and so-

The present results demonstrate that corrosion-induced vacancy injection occurs in the narrow potential range of active dissolution where steel is highly susceptible to IGSCC. The possible role of vacancies in GB embrittlement during IGSCC should therefore be considered. According to Neeraj et al. [23], aggregation of strain-induced vacancies led to nanovoids that they observed on fracture surfaces of H-embrittled pipeline steels. On the macroscale [59], considering the cohesive behavior of the crack tip, the existence of nanovoids close to GBs might reduce the GB cohesive strength, thereby shielding vacancy-enhanced plastic deformation within the grain boundary and leading to cleavage GB fracture [60,61].

# 4. Conclusions

MD simulations of nanoindentation experiments showed that the previously observed mechanical softening near corroded GBs is likely caused by vacancies, since the MD simulations show that vacancies explain the observed reduced critical load for dislocation nucleation. A role of absorbed hydrogen in softening can be dismissed, due to the very small concentration of H at the potential of anodic steel dissolution. Moreover, the MD calculations show that vacancies nucleate dislocations much more effectively than interstitial H at the same concentration, as the dislocation activation volume with atomic vacancies is about half that of Hinterstitials. Diffusion calculations further suggest that the vacancies derive from oxidation of silicon solute atoms at grain boundaries. Specifically, the importance of Si oxidation is supported by quantitative agreement between the measured critical load reduction close to the GB and the MD-predicted load reduction for a vacancy concentration equivalent to the bulk Si concentration. Vacancy diffusion also reasonably explains the thickness of the zone of enhanced plasticity surrounding GBs. The results help elucidate the mechanistic pathway linking alloy composition, corrosion electrochemistry, metal defects and local mechanical property changes. Because these processes occur in the narrow potential range where pipeline steel is vulnerable to high-pH SCC, there is a strong possibility that corrosion-induced vacancies play an important role in the SCC mechanism.

# **Declaration of Competing Interest**

The authors declare that they have no known competing financial interests or personal relationships that could have appeared to influence the work reported in this paper.

### Acknowledgments

This work was supported by the U.S. Department of Transportation, Pipeline and Hazardous Materials Safety Administration under Competitive Academic Agreement Program No. DTPH5614HCAP01 and 693JK31950003CAAP, the National Science Foundation (NSF) under contract DMR-1807545, and by the National Center for Supercomputing Applications Extreme Science and Engineering Discovery Environment XSEDE-allocation TG MSS170003 and MSS 190008. TP and LX also acknowledge the support by NSF under CMMI-1930093.

# Appendix A. Concentrations of hydrogen and vacancy-hydrogen defects at the experimental conditions

The equilibrium chemical potential of hydrogen interstitials is

$$\mu_{H} - \frac{1}{2}\mu_{H_{2}}^{0} = -F(\varphi - \varphi_{H})$$

where  $\mu_H$  is the H chemical potential in the metal,  $\mu_{H_2}^0$  is the chemical potential of H<sub>2</sub> gas at 1 atm pressure, F is Faraday's constant,  $\varphi$  is the applied potential (-0.52 V vs. Ag/AgCl reference electrode) and  $\varphi_H$  is the potential of the hydrogen electrode at the experimental pH 8.1 (-0.68 V vs. Ag/AgCl). From these values,  $\mu_H - \frac{1}{2}\mu_{H_2}^0 = -15$  kJ/mol, and the equilibrium H concentration is  $C_H = 2 \times 10^{-11}$ , normalized with the concentration of host atoms [62]. The equilibrium concentration of vacancy-hydrogen (Vac-H) defects is then

$$\frac{C_{V-H}}{C_V} = \frac{C_H}{C_H + z \exp\left(-\frac{h_b}{R_g T}\right)} \tag{A.1}$$

where  $C_V$  and  $C_{V-H}$  are the concentrations of vacancies and Vac-H defects, z=6 is the number of interstitial sites per Fe atom,  $h_h$ 

is the vacancy-hydrogen binding enthalpy, and  $R_g$  is the universal gas constant [63]. Besenbacher et al. found  $h_b$  to be 0.63 eV for binding of 1-2 H atoms per vacancy, from which  $C_{V-H}/C_V$  ratio is 0.1 [64]. However, it is unlikely that the equilibrium Vac-H concentration is approached experimentally in view of the very small H concentration of  $2 \times 10^{-11}$  (equivalent to an average H-H distance of about 1  $\mu$ m) [63,64]. Moreover, the estimated H concentration could be significantly smaller than the equilibrium value if cathodic water reduction and absorption kinetics were taken into account [65]. Therefore, at potentials of active Fe dissolution at most only a small fraction of vacancies would be associated with trapped hydrogen.

#### References

- [1] J.R. Scully, Environment-assisted intergranular cracking, MRS Bull. 24 (1999) 36-42.
- [2] J.L. Searles, P.I. Gouma, R.G. Buchheit, Stress corrosion cracking of sensitized AA5083 (Al-4.5Mg-1.0Mn), Metall. Mater. Trans. A 32 (2001) 2859–2867.
- [3] D.B. Wells, J. Stewart, A.W. Herbert, P.M. Scott, D.E. Williams, The use of percolation theory to predict the probability of failure of sensitised, austenitic stainless steels by intergranular stress corrosion cracking, Corrosion 45 (1989) 649–660.
- [4] N. Badwe, X. Chen, D.K. Schreiber, M.J. Olszta, N.R. Overman, E.K. Karasz, A.Y. Tse, S.M. Bruemmer, K. Sieradzki, Decoupling the role of stress and corrosion in the intergranular cracking of noble-metal alloys, Nat. Mater. 17 (2018) 887-893.
- [5] S.P. Knight, N. Birbilis, B.C. Muddle, A.R. Trueman, S.P. Lynch, Correlations between intergranular stress corrosion cracking, grain boundary microchemistry, and grain-boundary electrochemistry for Al-Zn-Mg-Cu alloys, Corros. Sci. 52 (2010) 4073–4080.
- [6] J. Beavers, T.A. Bubenik, Woodhead Publishing, Duxford UK, 2017, pp. 295-314.
- [7] R.D. Armstrong, A.C. Coates, Correlation between electrochemical parameters and stress corrosion cracking, Corros. Sci. 16 (1976) 423–433.
- [8] E. Wendler-Kalsch, The effects of film formation and mechanical factors on the initiation of stress corrosion cracking of unalloyed steels in carbonate solutions, Werkst. Korros. 31 (1980) 531–542.
- [9] R.N. Parkins, S. Zhou, The stress corrosion cracking of C-Mn steel in CO<sub>2</sub>-HCO<sub>3</sub><sup>-</sup>-CO<sub>3</sub><sup>2-</sup> solutions. I. Stress corrosion data, Corros. Sci. 39 (1997) 159–173.
- [10] R.N. Parkins, Predictive approaches to stress-corrosion cracking failure, Corros. Sci. 20 (1980) 147–166.
- [11] J.Q. Wang, A. Atrens, Measurement of grain boundary composition for X52 pipeline steel, Acta Mater. 46 (1998) 5677–5687.
- [12] D. Yavas, A. Alshehri, P. Mishra, P. Shrotriya, A.F. Bastawros, K.R. Hebert, Morphology and stress evolution during the initial stages of intergranular corrosion of X70 steel, Electrochim. Acta. 285 (2018) 336–343.
- [13] D. Yavas, P. Mishra, A. Alshehri, P. Shrotriya, K.R. Hebert, A.F. Bastawros, Nanoindentation study of corrosion-induced grain boundary degradation in a pipeline steel, Electrochem. Commun. 88 (2018) 88–92.
- [14] E.K. Njeim, D.F. Bahr, Atomistic simulations of nanoindentation in the presence of vacancies, Scripta. Mater. 62 (2010) 598–601.
- [15] I. Salehinia, D.F. Bahr, The impact of a variety of point defects on the inception of plastic deformation in dislocation-free metals, Scripta. Mater. 66 (2012) 339–342.
- [16] A. Barnoush, H. Vehoff, In situ electrochemical nanoindentation: a technique for local examination of hydrogen embrittlement, Corros. Sci. 50 (2008) 259–267.
- [17] A. Barnoush, H. Vehoff, Recent developments in the study of hydrogen embrittlement: hydrogen effect on dislocation nucleation, Acta Mater. 58 (2010) 5274–5285.
- [18] A. Bastawros, Fundamental Mechanochemistry-based Detection of Early Stage Corrosion Degradation of Pipeline Steels, Project Final report, Pipeline and Hazardous Materials Safety Administration, Department of Transportation, 2020.
- [19] S. Parida, D. Kramer, C.A. Volkert, H. Rösner, J. Erlebacher, J. Weissmüller, Volume change during the formation of nanoporous gold by dealloying, Phys. Rev. Lett. 97 (2010) 035504.
- [20] K. Sakaki, T. Kawase, M. Hirato, M. Mizuno, H. Araki, Y. Shirai, M. Nagumo, The effect of hydrogen on vacancy generation in iron by plastic deformation, Scripta. Mater. 55 (2006) 1031–1034.
- [21] K. Takai, H. Shoda, H. Suzuki, M. Nagumo, Lattice defects dominating hydrogen-related failure of metals, Acta Mater. 56 (2008) 5158–5167.
- [22] A. Oudriss, J. Creus, J. Bouhattate, E. Conforto, C. Berziou, C. Savall, X. Feugas, Grain size and grain-boundary effects on diffusion and trapping of hydrogen in pure nickel, Acta Mater. 60 (2012) 6814–6828.
- [23] T. Neeraj, R. Srinivasan, J. Li, Hydrogen embrittlement of ferritic steels: observations on deformation microstructure, nanoscale dimples and failure by nanovoiding, Acta Mater. 60 (2012) 5160–5171.
- [24] S.Z. Li, Y.G. Li, Y.C. Lo, T. Neeraj, R. Srinivasan, X.D. Ding, J. Sun, L. Qi, P. Gumbsch, J. Li, The interaction of dislocations and hydrogen-vacancy complexes and

- its importance for deformation-induced proto nano-voids formation in  $\alpha$ -Fe, Int. J. Plast. 74 (2015) 175–191.
- [25] C. Yang, C.T. Lo, A.F. Bastawros, B. Narasimhan, Measurements of diffusion thickness at polymer interfaces by nanoindentation: a numerically calibrated experimental approach, J. Mater. Res. 24 (2009) 970–992.
- [26] B. Taljat, T. Zacharia, G.M. Pharr, Pile-up behavior of spherical indentations in engineering materials, MRS Proc. 522 (1998) 33–38.
- [27] D. Yavas, P. Mishra, A.F. Bastawros, K.R. Hebert, P. Shrotriya, Characterization of sub-surface damage during the early stage of stress corrosion cracking by nano indentation, in: Y. Zhu, A. Zehnder (Eds.), Experimental and Applied Mechanics, Volume 4. Conference Proceedings of the Society for Experimental Mechanics Series, Springer, Cham, 2017, doi:10.1007/978-3-319-42028-8\_5.
- [28] H. Van Swygenhoven, Grain boundaries and dislocations, Science 296 (2002) 66-67.
- [29] S. Plimpton, Fast parallel algorithms for short-range molecular dynamics, J. Comput. Phys. 117 (1995) 1–19.
- [30] M.I. Mendelev, S. Han, D.J. Srolovitz, G.J. Ackland, D.Y. Sun, M. Asta, Development of new interatomic potentials appropriate for crystalline and liquid iron, Philos. Mag. 83 (2003) 3977–3994.
- [31] A. Ramasubramaniam, M. Itakura, E.A. Carter, Interatomic potentials for hydrogen in  $\alpha$ -iron based on density functional theory, Phys. Rev. B 79 (2009) 174101
- [32] A. Stukowski, Visualization and analysis of atomistic simulation data with OVI-TO-the open visualization tool, Model. Simul. Mater. Sci. 18 (2009) 015012.
- [33] S. Taketomi, R. Matsumoto, N. Miyazaki, Atomistic study of hydrogen distribution and diffusion around a {112}< 111>edge dislocation in alpha iron, Acta Mater. 56 (2008) 3761–3769.
- [34] C.A. Schuh, J.K. Mason, A.C. Lund, Quantitative insight into dislocation nucleation from high-temperature nanoindentation experiments, Nat. Mat. 4 (2005) 617–621.
- [35] K.L. Johnson, Contact Mechanics, Cambridge University Press, Cambridge UK, 1985.
- [36] W.W. Gerberich, S.K. Venkataraman, H. Huang, S.E. Harvey, D.L. Kohlstedt, The injection of plasticity by millinewton contacts, Acta Metall. Mater. 43 (1995) 1569–1576.
- [37] S. Suresh, T.G. Nieh, B.W. Choi, Nano-indentation of copper thin films on silicon substrates, Scripta Mater. 41 (1999) 951–957.
- [38] A. Gouldstone, H.J. Koh, K.Y. Zeng, A.E. Giannakopoulos, S. Suresh, Discrete and continuous deformation during nanoindentation of thin films, Acta Mater. 48 (2000) 2277–2295.
- [39] M. Pang, D.F. Bahr, Thin-film fracture during nanoindentation of a titanium oxide film-titanium system, J. Mater. Res. 16 (2001) 2634–2643.
- [40] Y. Shibutani, A. Koyama, Surface roughness effects on the displacement bursts observed in nanoindentation, J. Mater. Res. 19 (2004) 183–188.
- [41] L. Lu, R. Schwaiger, Z.W. Shan, M. Dao, K. Lu, S. Suresh, Nano-sized twins induce high rate sensitivity of flow stress in pure copper, Acta Mater. 53 (2005) 2169–2179.
- [42] R.J. Asaro, S. Suresh, Mechanistic models for the activation volume and rate sensitivity in metals with nanocrystalline grains and nano-scale twins, Acta Mater. 53 (2005) 3369–3382.
- [43] G. Monnet, D. Terentyev, Structure and mobility of the ½ <111>{112} edge dislocation in BCC iron studied by molecular dynamics, Acta Mater 57 (2009) 1416–1426.
- [44] G. Domain, G. Monnet, Simulation of screw dislocation motion in iron by molecular dynamics simulations, Phys. Rev. Lett. 95 (2005) 215506.
- [45] K. Tapasa, Y.N. Osetsky, D.J. Bacon, Computer simulation of interaction of an edge dislocation with a carbon interstitial in alpha-iron and effects on glide, Acta Mater. 55 (2007) 93–104.
- [46] P.C. Wo, L. Zuo, A.H.W. Ngan, Time-dependent incipient plasticity in Ni3Al as observed in nanoindentation, J. Mater. Res. 20 (2005) 489–495.
- [47] C.A. Schuh, A.C. Lund, Application of nucleation theory to the rate dependence of incipient plasticity during nanoindentation, J. Mater. Res. 19 (2004) 2152–2158.
- [48] W.A. Spitzig, The effects of orientation, temperature and strain rate on deformation of Fe-0.16 wt.% Ti single crystals, Mater. Sci. Eng. 12 (1973) 191–202.
- [49] W.A. Spitzig, A.S. Keh, Orientation dependence of the strain-rate sensitivity and thermally activated flow in iron single crystals, Acta Metall. 18 (1970) 1021–1033.
- [50] S. Wang, N. Hashimoto, Y. Wang, S. Ohnuki, Activation volume and density of mobile dislocations in hydrogen-charged iron, Acta Mater. 61 (2013) 4734–4742.
- [51] A.F. Bastawros, Analysis of deformation-induced crack tip toughening in ductile single crystals by nano-indentation, Int. J. Solids Struct. 43 (24) (2006) 7358–7370.
- [52] L. Xiong, G. Tucker, D.L. McDowell, Y. Chen, Coarse-grained atomistic simulation of dislocations, J. Mech. Phys. Solids 59 (2) (2011) 160–177.
- [53] L. Xiong, D.L. McDowell, Y. Chen, Nucleation and growth of dislocation loops in Cu, Al, and Si by a concurrent atomistic-continuum method, Scripta Mater. 67 (7-8) (2012) 633–636.
- [54] L. Xiong, S. Xu, D.L. McDowell, Y. Chen, Concurrent atomistic-continuum simulations of dislocation-void interactions in FCC crystals, Int. J. Plast. 65 (2015) 33–42.
- [55] S. Xu, L. Xiong, Y. Chen, D.L. McDowell, Sequential Slip transfer of mixed-character dislocation across sigma-3 coherent twin boundary in FCC metals: a concurrent atomistic-continuum study, Npi Comput. Mater. 2 (1) (2016) 1–9.

- [56] X. Chen, W. Li, L. Xiong, Y. Li, S. Yang, Z. Zheng, D.L. McDowell, Y. Chen, Ballistic-diffusive phonon heat transport across grain boundaries, Acta Mater. 136 (2017) 355–365.
- [57] X. Chen, L. Xiong, D.L. McDowell, Y. Chen, Effects of phonons on mobility of dislocations and dislocation arrays, Scripta Mater. 137 (2017) 22-26.
- [58] M.I. Mendelev, Y. Mishin, Molecular dynamics study of self-diffusion in BCC Fe, Phys. Rev. B 80 (2009) 144111.
- [59] V. Tvergaard, J.W. Hutchinson, The relation between crack growth resistance and fracture process parameters in elastic–plastic solids, J. Mech. Phys. Solids  $40\ (1992)\ 1377-1397.$
- [60] X. Zhou, B. Ouyang, W.A. Curtin, J. Song, Atomistic investigation of the influence of hydrogen on dislocation nucleation during nanoindentation in Ni and Pd, Acta Mater. 116 (2016) 364-369.
- [61] D. Yavas, X. Shang, W. Hong, A.F. Bastawros, Utilization of nanoindentation to examine bond line integrity in adhesively bonded composite structures, Int. J. Fract. 204 (2017) 101-112.
- [62] Y. Fukai, The Metal-Hydrogen System. Basic Bulk Properties, 2nd Ed., Springer, Berlin, 2005.

- [63] S.M. Myers, S.T. Picraux, R.E. Stoltz, Defect trapping of ion-implanted deuterium in Fe, J. Appl. Phys. 50 (1979) 5710–5719.
  [64] F. Besenbacher, S.M. Myers, P. Nordlander, J.K. Nørskov, Multiple hydrogen occupancy of vacancies in Fe, J. Appl. Phys. 61 (1987) 1788–1794.
  [65] A. Turnbull, Perspectives on hydrogen uptake, diffusion and trapping, Int. J. Hydrog. Energy 40 (2015) 169561 16970.